ACSNANO

www.acsnano.org

Holey and Wrinkled Flash Graphene from Mixed Plastic Waste

Kevin M. Wyss, Weiyin Chen, Jacob L. Beckham, Paul E. Savas, and James M. Tour*

Cite This: https://doi.org/10.1021/acsnano.2c00379 Read Online

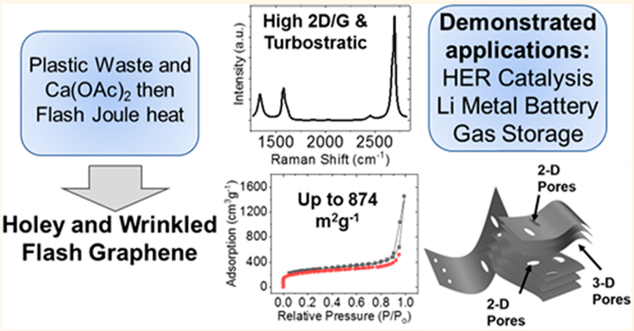

ABSTRACT: **High surface area varieties of graphene have captured significant attention, allowing for improved performance in a variety of applications. However, there are challenges facing the use of graphene in these applications since it is expensive and difficult to synthesize in bulk. Here, we leverage the capabilities of flash Joule heating to synthesize holey and wrinkled flash graphene (HWFG) in seconds from mixed plastic waste feedstocks, using *in situ* salt decomposition to produce and stabilize pore formation during the reaction. Surface areas as high as 874 $m^2\ g^{-1}$ are obtained, with characteristics of micro-, meso-, and macroporosities. Raman spectroscopy confirms the wrinkled and turbostratic nature of the HWFG. We demonstrate HWFG applications in its use as a metal-free hydrogen evolution reaction electrocatalyst, with excellent stability, competitive overpotential, and Tafel slope; in a Li-metal battery anode allowing for stable and high discharge rates; and in a material with high gas adsorption. This represents an upcycle of mixed plastic waste, thereby affording a valuable route to address this pressing environmental pollutant concern.**

KEYWORDS: *holey and wrinkled flash graphene, flash graphene, mixed plastic waste, flash Joule heating, turbostratic graphene*

Graphene has attracted much interest because of its high physical strength, low density, chemical robustness, and extreme electrical mobility.[1−4] Because of these impressive properties, graphene has been implemented in an ever-increasing number of applications, from composites and coatings to energy storage devices and sensors.[5−8] A more recent scientific thrust has been to investigate the various arrangements of graphene sheets or modifications to the graphene sheet structure. For example, low-angle stacking of graphene can lead to superconductive behavior,[9] and corrugated or strained three-dimensional (3D) arrangements of graphene sheets show pseudomagnetic fields or Hall effects.[10,11] Additionally, porous forms of graphene, with either 2D or 3D arrangements, result in holey or wrinkled graphene, respectively. Three-dimensional arrangements are termed porous, wrinkled, rippled, or corrugated graphenes. These 3D wrinkled materials often demonstrate significant improvements in surface area and thus lower the loading concentrations for use in applications when compared to other forms of graphene.[12,13]

Synthesis of holey and wrinkled graphene (HWG) is difficult; a potentially scalable and industrially viable route for bulk synthesis is needed. Laboratory-scale synthesis of a holey form of HWG begins with aqueous solutions of graphene oxide (GO), which are then chemically, catalytically, or thermally treated to etch the GO sheets with intrasheet or two-dimensional (2D) in-plane pores. The in-plane defects induced in the GO sheets act as nucleation sites for hole etching.[14] Common etching strategies include the use of strong peroxides or microwave/infrared irradiation of metal nanoparticles or oxidizing agents.[15] To form 3D pores present in crumpled HWG, GO is the predominant starting material. Poly(methyl methacrylate) beads, SiO_2 nanoparticles, or other nanomaterials have been used as templating agents.[16]

Once 2D or 3D pores are present on the GO sheets, varying combinations of solvothermal reaction, lyophilization, and reduction (either *via* CVD or chemically) are used to produce the high surface area HWG.[17] The use of GO has two drawbacks: the synthesis of the relatively expensive GO is chemically intensive, and oxygen functionalities are present in the final product that can negatively impact its properties, such as conductivity.[18] As applications for HWG continue to be demonstrated, a scalable method to produce high-quality

Received: January 12, 2022
Accepted: April 19, 2022

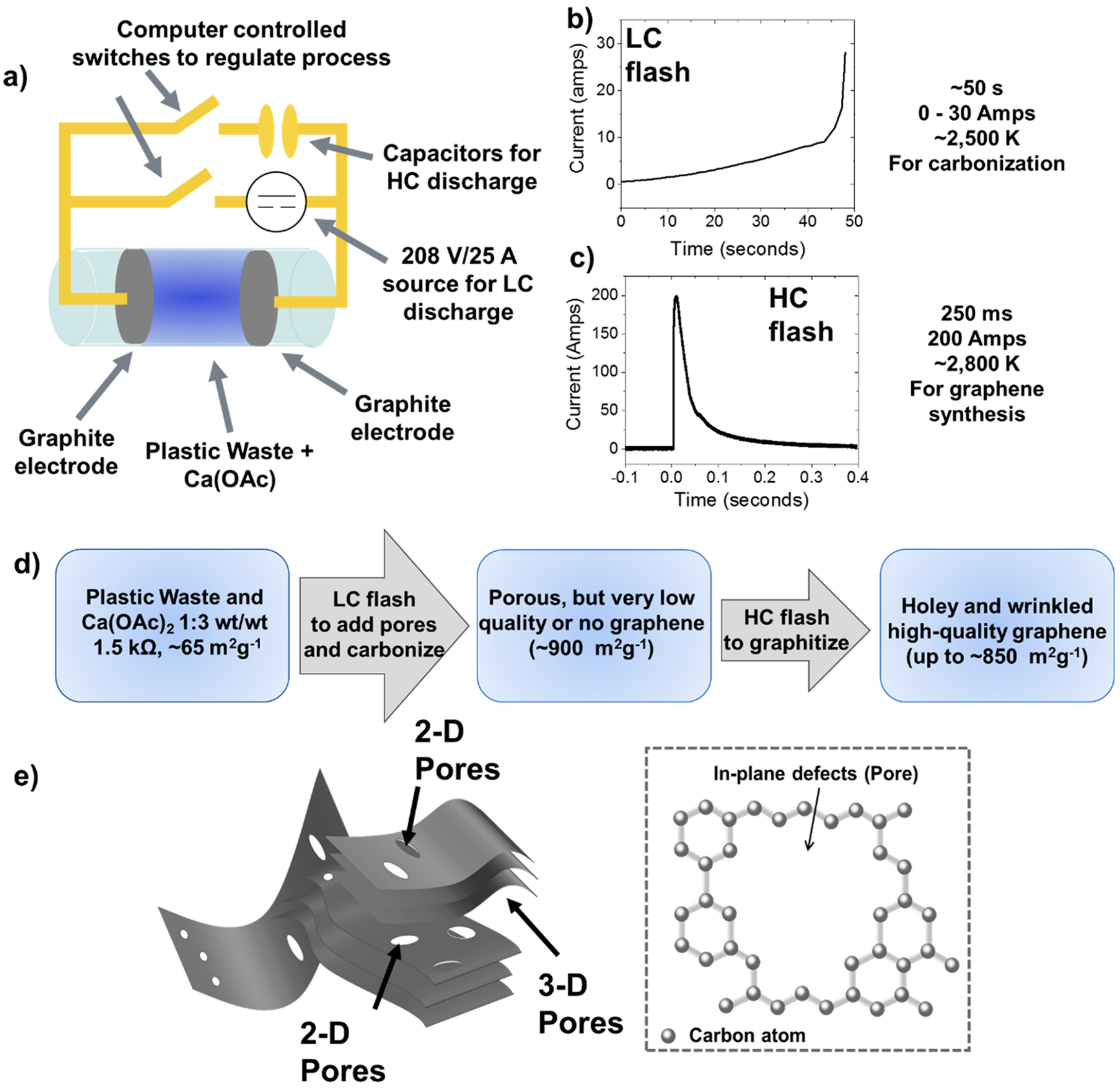

Figure 1. Diagram showing (a) an FJH schematic composed of a 30 A, 208 V rectified power supply and a 128 mF capacitor allowing for LC and HC heating to be used in tandem. Current profiles for (b) LC and (c) HC methods and (d) a workflow for the synthesis of HWFG. A conductive additive of 5−8 wt % such as metallurgical coke or carbon black is necessary to reduce the resistance of the mixture. (e) Diagram showing 2D and 3D pores present in turbostratic HWFG.

HWG remains elusive. HWG often displays high oxygen elemental content and no Raman 2D peak, suggesting a lack of long-range graphene order.[19,20]

Here, flash Joule heating (FJH) is used to synthesize holey and wrinkled flash graphene (HWFG) from virgin plastic and single-source or mixed plastic waste (PW) in a simple two-step method using no harsh etching or templating agents, solvothermal reactions, lyophilization, furnaces, or inert gases. The process leads to both physical and chemical activation *via* the *in situ* decomposition of alkali ionic compounds during the FJH process, producing a 15-fold increase in surface area for HWFG when compared to the starting material. The activation stabilizes the porous carbon during the graphitization of plastic, inducing the high surface area formation and generating high-quality HWFG. Both 2D and 3D hierarchical pores are observed, with high surface areas (650−874 m^2 g^{-1}) and a wide pore size distribution, spanning micro-, meso-, and macroporosity. Applications of HWFG in electrocatalysis, Li-metal battery anodes, and gas uptake are demonstrated, and a synthetic mechanism is proposed.

FJH is a process in which electrical current is discharged through a resistive carbon feedstock.[21,22] Since the carbon feedstock has a nonzero resistance, heat is produced in proportion to the square of the magnitude of the current. The FJH process uses capacitors that can output hundreds of amps within milliseconds to produce rapid high-current discharges that are passed through almost any carbon feedstock to synthesize graphene.[23] Temperatures more than 2800 K can be reached with heating rates of 10^5 K s^{-1} or faster. Cooling rates are similarly rapid at 10^4 K s^{-1}. At these high temperatures, the feedstock is converted to the thermodynamically preferred sp^2-hybridization of a graphene sheet. Because of the rapid cooling rates, the formed graphene sheets are kinetically trapped in a disordered state in which they are rotationally mismatched from one another, rather than neatly stacking in an AB manner as would be derived from graphite exfoliation to few-layered graphene nanoplatelets.[24] This rotational disorder, also known

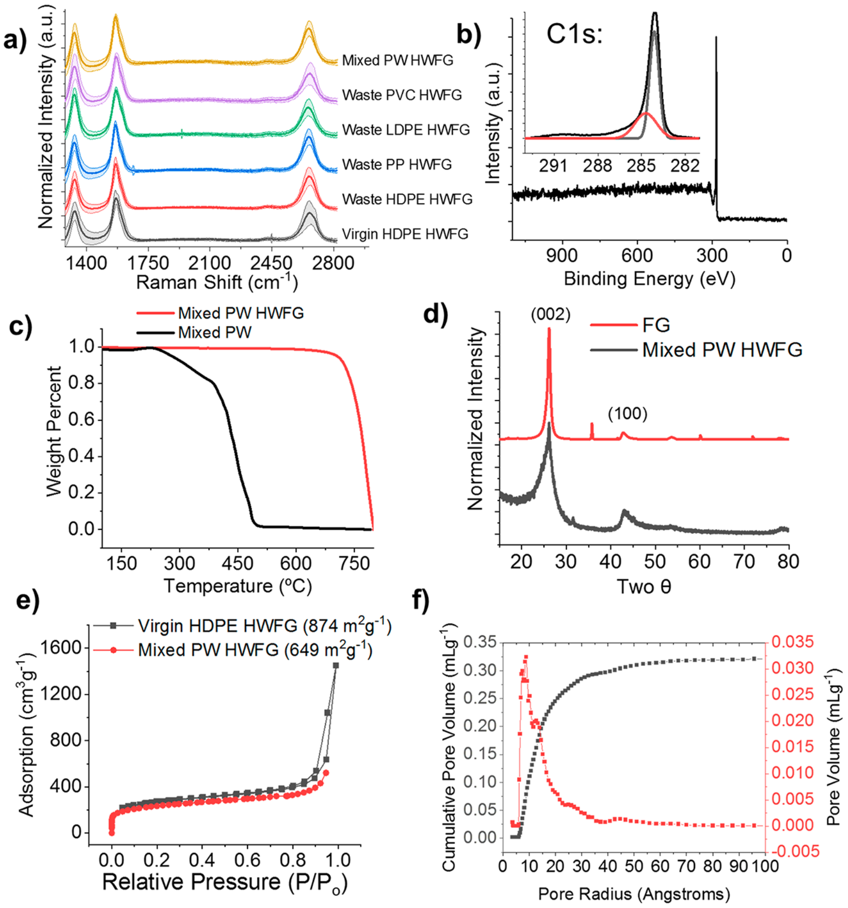

Figure 2. Characterization of HWFG derived from PW using (a) Raman spectroscopy, showing the average of a 100 spectra map, with standard deviation indicated by the shaded area in each spectra. (b) Mixed PW-derived HWFG as analyzed by low-resolution XPS survey spectra showing high carbon elemental purity, with the inset high-resolution C 1s spectra showing solely sp^2- and sp^3-hybridization (the gray peak is fit to sp^2; the red peak is fit to sp^3; and the black peak is experimental data). (c) TGA of WP-derived HWFG (air, 80 mL min^{-1}) shows an increase in thermal stability compared to the starting material WP, and (d) powder XRD comparing HWFG to previously synthesized FG demonstrating a larger fwhm in the (002) peak. (e) BET isotherms for virgin HDPE and mixed PW-derived HWFG and (f) pore size distribution for the virgin HDPE HWFG sample.

as turbostratic stacking, results in a significant decrease in van der Waals attractions between the electron-rich and electron-poor regions of the aromatic rings.[24] This mismatch increases the interlayer spacing, facilitating exfoliation to few- or monolayer graphene during composite formation or dissolution. The high quality and elemental purity of FG, as well as the scalability of the process, have been well studied.[25,26] Frustratingly, the surface area of the FG is generally only 60 and 200 m^2 g^{-1}, far lower than the theoretical maximum surface area for single-sheet graphene of ~2600 m^2 g^{-1}.[27] The surface area of FG remains low even if high surface area starting carbon feedstocks are used.

RESULTS AND DISCUSSION

Inspired by the use of blowing agents in the synthesis of porous polymers such as polyurethane foam, we began exploring strategies for the synthesis of HWFG by FJH. Pores are formed in the polyurethane foam when isocyanates or azodicarbonamides decompose in the polyurethane melt.[28] This decomposition causes the evolving gases to physically form pores in the polymer. Addition of salts such as KOH can decompose to etch pores in carbon feedstocks during thermal synthetic methods in a chemical activation process.[29] This strategy has been employed in production of very high surface area amorphous carbon materials from carbon feedstocks using heated tube furnaces under an inert atmosphere.[30] The FJH strategy demonstrated here combines both physical and chemical activation *in situ* in a FJH reaction. Calcium acetate, $Ca(OAc)_2$, undergoes a two-step decomposition to evolve acetone and then, at higher temperatures, CO_2, resulting in physical blowing and chemical etching of pores. The residual CaO byproduct is deposited in the pores and appears important to preserving the porous structure during graphitization. We have found that this decomposition can be triggered inside a carbon-containing host during FJH, resulting in the formation of a porous product. Potassium salts were not used since water-reactive potassium metal could form during the FJH process and thereby could cause fires upon aqueous workup. This problem could be exacerbated upon scaleup. PW was the feedstock for this FJH process.

The FJH process was carried out using a dual-capable FJH station, capable of both high-current, short-duration reactions and lower current, longer duration reactions. A simplified schematic of the FJH system is shown in Figure 1a. Further details can be found in the Supporting Information and Figure S1. First, a low current (LC), long-duration flash, at 208 V, is applied to the mixture of PW and $Ca(OAc)_2$ in a reaction tube with the current increasing from 0.1 A to ~25 A, for ~50 s, at

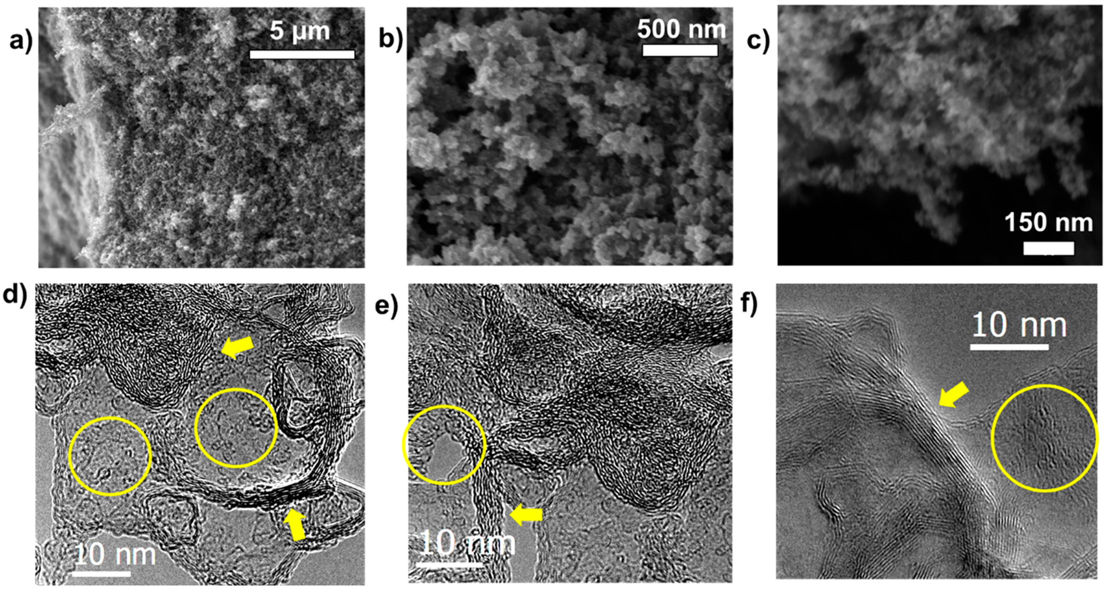

Figure 3. Electron microscopy of HWFG derived from mixed PW. (a−c) SEM images showing 3D macroporosity as well as (d−f) TEM images, showing 2D meso- and microporosity. Etched micro- and mesopores are marked with circles, while the graphene lattice fringe is marked with an arrow in the TEM images.

which point a homogeneous glow is observed (current discharge shown in Figure 1b). The current increases because the resistance of the PW/Ca(OAc)$_2$ mixture decreases as the carbonization takes place. The initial resistance, 1.5 kΩ, results in a longer duration carbonization than previously reported for FJH conversion of plastics to FG. The initial resistance of PW is lowered by adding 5 wt % conductive carbon black to the PW/Ca(OAc)$_2$ mixture. The carbonization results in temperatures reaching ~2500 K and generates amorphous carbon (Figure S2).[22] After the carbonization, graphitization is accomplished by a high-current (HC), short-duration flash supplied by 60 mF capacitors that were charged to 100 V and discharged for 250 ms (current discharge shown in Figure 1c). An overall process workflow is shown in Figure 1d. After the second discharge, HWFG mixed with CaO salt is obtained. The CaO salt can be removed from the HWFG by soaking it in weak aqueous acetic or hydrochloric acid (1 M) overnight, followed by filtration and rinsing. A schematic showing how pores and wrinkles may be present in the produced HWFG is shown in Figure 1e.

For initial tests, virgin high-density polyethylene (HDPE) was used, but later trials showed that several PW streams convert well to HWFG using this method. Further, a realistic stream of PW, containing 40% HDPE, 20% polypropylene, 10% polyethylene terephthalate (PET), 10% polyvinyl chloride (PVC), and 20% low-density polyethylene (LDPE), was tested. PET by itself does not convert well to HWFG and produces low surface area graphene (Figure S3). Optimization of the ratio of PW to an activating agent (Figure S4) shows that a 3:1 w/w ratio of Ca(OAc)$_2$ to PW is preferred.

Following successful synthesis of the HWFG, the material was characterized using Raman spectroscopy, X-ray photoelectron spectroscopy (XPS), and powder X-ray diffraction (XRD). Raman spectroscopy confirmed the conversion of PW into graphene. Figure 2a shows the average spectra of a 1 mm^2 Raman spectral map consisting of 100 spots. For most PW feedstocks except PET, high-quality HWFG is produced. The conversion yield of polymeric carbon to graphene carbon ranges from 9% to 13% depending on the feedstock. To increase the yield, we are currently experimenting with semisealed systems that retain the polymeric carbon in the reaction area for longer durations, minimizing the mass lost to off-gassing. The volatiles are not currently captured, but industrial production would require capture and utilization. These studies are in progress. For the remaining solids in the reactor, 95−99% of the recovered solid product is identifiable as graphene as shown by the prominent 2D peak (2690 cm^{-1}) and G peak (1580 cm^{-1}). The D peak occurs at 1350 cm^{-1}, corresponding to the defects occurring within the sheet of HWFG.[31] In the HWFG, a large D peak is observed, attributable to the occurrence of 2D in-plane non-sp^2-hybridized edges or point defects. Elemental purity was analyzed using XPS, as shown in Figure 2b. After rinsing of the HWFG, no oxygen or calcium was detected during the low-resolution XPS survey scans, indicative of the highly pure nature of the HWFG sheets. High-quality graphene and large-scale sp^2-hybridization are chemically stable; strong oxidizing agents and harsh acidic agents are required for Hummer's process to oxidize graphene. The molarities of acid used here to rinse the product and the fact that no oxidizing agent is present during that step allow the graphene to remain low in oxygen functionalities. After the rinsing and drying steps, the graphene is stable and resistant to atmospheric oxidation. Using high-resolution XPS and peak deconvolution to examine the C 1s binding region, only C−C and C═C bond types are detected with peaks occurring at 284.6 and 284.1 eV, respectively. No C−O, O−C−O, or C═O character is found during the C 1s deconvolution, but if present these peaks would occur between 285.5 and 288.5 eV. Further, $\pi-\pi^*$ interactions are present, indicating the aromatic portion of the bonding as visible in a small, broad peak at 291 eV. After the LC discharge, carbon and oxygen functionalities are detected (O 1s at 533 eV and Ca 2p at 346 eV), and calcium and oxygen atoms are still found on the surface after the HC discharge (Figure S5). However, after HC discharge and acid rinsing, these peaks in the low-resolution XPS survey scans disappear.

Characterization of the thermal stability of the HWFG was conducted using thermogravimetric analysis (TGA). High thermal stability (90% remaining at 750 °C) and a single degradation event were observed, signifying complete conversion of the PW into HWFG (Figure 2c). Powder XRD was used to study the crystallinity of the HWFG (Figure 2d). As previously reported for turbostratic FG products, a downward shift in the (002) peak is observed from 26.7° in graphite to 26.1° in HWFG, which is attributable to the increase in interlayer spacing. Further, the (002) peak is observed to have a much larger full-width at half-maximum (fwhm) than other FG products, 2.84° here as compared to previously reported 1.11°.[25] This is likely due to the 3D porous and wrinkled arrangement of HWFG sheets, resulting in a large distribution of stacking environments and therefore larger interlayer spacings and crystal domains.

To examine the porosity and surface area of the HWFG, Brunauer−Emmett−Teller (BET) analysis was conducted using N_2 gas at 78 K. Isotherms (Figure 2e) indicate that the surface area of HWFG derived from virgin HDPE can be as high as 874 m^2 g^{-1}. HWFGs derived from PW are all above 700 m^2 g^{-1}, except for PET, which had an extremely low surface area of 91.2 m^2 g^{-1}. Mixed PW HWFG had a surface area of 649 m^2 g^{-1}. It is not clear why virgin HDPE formed a higher surface area than PW; the HDPE powder had a smaller grain size, possibly resulting in a more homogeneous mix of reagents and therefore superior activation during the FJH process. Further, PW contains PET, which does not readily convert to HWFG, lowering the specific surface area of the produced HWFG. A broad, polydisperse pore size distribution was observed for all HWFG products, spanning the micro- and mesoporous regimes, with 36% of the cumulative pore volumes coming from microporous contributions (Figure 2f). Microporosity is known to positively impact sensing and adsorption capabilities of carbonaceous adsorbents.[32,33] Because of the high surface area and high micropore volume, the gas adsorption was tested. When compared to previously synthesized FG, HWFG demonstrated a 10-fold increase in CO_2 uptake, sorbing 15.3 wt %, or 3.47 mmol g^{-1} at 1 bar and 298 K (Figure S6) for possible use in flue gas CO_2 capture.

As discussed above, PET did not form HWFG but rather was converted into low surface area FG (Figure S3). This might be due to the higher melting point of PET when compared to the other polymers, 260 °C for PET as opposed to 160 °C for PP and 120 °C for HDPE, impacting the kinetics of the reaction, but further mechanistic study is required.

Confirmation of the porosity of HWFG is possible using SEM and TEM imaging. SEM imaging (Figure 3a−c) shows the hierarchical porous arrangement and rough surface that is present in the HWFG. Using TEM imaging, a better understanding of the arrangement of the graphene sheets emerges. As shown in Figure 3d−f, the lattice fringe of the graphene can be observed, indicating the crystallinity that is present. The interlayer spacing of 0.356 nm was determined from the intensity profile of the lattice fringe. This is significantly larger than what is observed in graphite, 0.337 nm, and even larger than what is reported for other turbostratic graphene interlayer spacings, 0.345−0.351.[21] The layering is disrupted and not as regularly defined as in FG. On the basis of the evidence, synthesis in the presence of $Ca(OAc)_2$ results in increased defects, further disrupting the van der Waals interactions of the sheets. The turbostratic stacking of the HWFG is confirmed using selected area electron diffraction (SAED), which shows multiple overlaid lattices, confirming the rotational disorder in the sheet stacking (Figure S7). Figure 3f shows corrugated, wrinkled few-layer turbostratic graphene, which contributes 3D pores. Because of the observed increase in interlayer spacing, the dispersibility of HWFG in a 1% Pluronic F-127 surfactant assisted aqueous systems through sonication was studied. The HWFG dispersed extremely well, better than in previous reports (Figure S8).[21−23] To convey the possible scalability of our approach and compare the properties of HWFG to other high surface area graphene products and methods recently published, see Table S1.

The LC FJH step is estimated to require 21 kJ/g of material heated.[22] Thus, because of the ratio of $Ca(OAc)_2$ to plastic, 84 kJ/g of plastic is required to convert it to the high surface area amorphous intermediate. The HC FJH graphitization step is estimated to require 13 kJ/g of amorphous carbon.[22] However, only 0.1 g of the initial 1 g of plastic undergoes the HC FJH discharge. Thus, an estimated 85.3 kJ/g of electricity is required to convert 1 g of plastic into the high surface area HWFG. Using \$0.02/kWh, the west Texas industrial rate, the electricity cost would be \$474 per ton.

The concern can be raised that CO_2 evolution during the FJH process is counterproductive to the upcycling goal of converting plastic into HWFG. While CO_2 is certainly evolved during the production steps, it is important to study and compare all steps of the synthetic method to alternative processes. The major generation of CO_2 during the FJH process arises from the electricity required in the current discharge and the CO_2 produced from the $Ca(OAc)_2$ degradation. The FJH process requires 85.3 kJ/g of electricity and produces 0.27 g of CO_2 for every 1 g of $Ca(OAc)_2$ that degrades during the FJH process. For the 85.3 kJ/g used, an estimated 10.23 g of CO_2 is produced, according to the Argonne National Lab GREET database for U.S. mixed source electricity.[34] Further, because of the degradation of $Ca(OAc)_2$ to form CO_2, an additional 1.7 g of CO_2 is evolved for every 1 g of HWFG synthesized. Calculating CO_2 contributions from the remainder of the HWFG life-cycle synthesis (such as the CO_2 produced during production of HDPE, $Ca(OAc)_2$, or carbon black, among other indirect contributions) is outside the current scope of the project. However, it becomes clear that the CO_2 evolved during the FJH process from $Ca(OAc)_2$ degradation will be relatively small when compared to the CO_2 produced during the rest of the process. Few comprehensive life-cycle assessments (LCAs) are currently published for the synthesis of graphene, and none are available on the synthesis of porous, wrinkled, or holey graphene. A number of LCAs exist for the synthesis of graphene oxide, which is commonly used to synthesize high surface area graphene. In the literature, LCAs that estimated production of CO_2 as a result of graphene synthesis ranged from 86 to 320 g of CO_2 produced for every 1 g of graphene product.[35−37] These values are provided for reference; a complete LCA has not been conducted for this process, so we cannot directly compare the FJH cumulative emissions to other current processes or draw conclusions if the FJH process produces more or less CO_2 over the life cycle. Rather, we hope to illustrate that the 1.7 g of CO_2 evolved directly from the $Ca(OAc)_2$ per 1 g of HWFG synthesized is minor compared to other processes.

Research continued to further optimize the HWFG formation process by eliminating the dilute acid rinse step. A

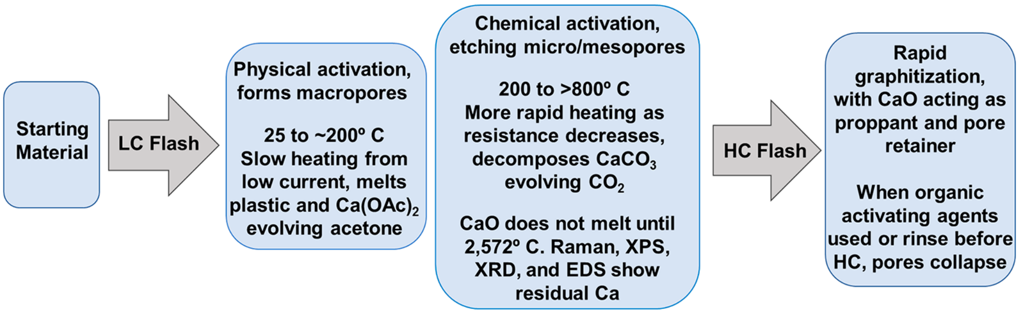

Figure 4. Scheme showing the proposed mechanistic phases for HWFG formation.

well-known industrial blowing agent, azodicarbonamide, was tested.[38] Azodicarbonamide degrades at 225 °C, producing NH_3, CO, CO_2, and N_2. We observed that a high surface area amorphous carbonized plastic product of 753 m^2 g^{-1} is produced following the LC discharge step; however a different morphology was observed than when $Ca(OAc)_2$ was used as the activating agent (Figure S9). However, following the HC graphitization step, the surface area drops dramatically to that of FG. In addition, the porous surface morphology is no longer observed after the HC discharge through SEM; thus, azodicarbonamide was not effective at maintaining the high surface area. Another mechanistic indicator during the optimization of the process was the failure of PET to convert to HWFG; instead, it formed a low surface area FG. Despite using a process like the one used for the other polymers, PET, both virgin and PET from different sources, consistently produced very low surface areas (70−100 m^2 g^{-1}) and a morphology corresponding to that of FG not HWFG.

Considering all this evidence, a mechanism for the synthesis of HWFG is theorized as follows: during the LC discharge, the mixed PW melts between 115 and 170 °C. Because of the high initial resistance of the sample mixture, slow heating is initially observed, allowing for homogeneous melting. Second, the $Ca(OAc)_2$ decomposes to form $CaCO_3$ and acetone gas at ~165 °C. This evolution of gas functions like a traditional industrial blowing agent, producing larger macropores within the melt. The LC discharge continues heating the sample and carbonizing the polymer feedstock as the temperature reaches and surpasses ~400 °C. As heating continues, the $CaCO_3$ degrades to form CaO and CO_2 at 840 °C. Raman spectroscopy confirms the conversion of $Ca(OAc)_2$ to CaO after the LC discharge step (Figure S10). The CO_2 etches the carbon framework, making micro- and mesopores.[39−41] The CaO is stable at 2800 °C and remains in the HWFG, which is now porous from the activation. The CaO is deposited within the framework of the porous carbon, functioning as proppant to maintain the pores and high surface area, through the HC discharge. The presence of CaO even after the HC step is confirmed using energy-dispersive X-ray spectroscopy (EDS) concurrently with SEM imaging. These scans (Figure S11) demonstrate an even coating of CaO is present on the surface of the unrinsed HWFG.

The importance of the residual CaO to preserve the porous structure is established through multiple experiments. First, when azodicarbonamide was used as the activating agent, a high surface area is observed after the LC discharge. However, after the HC discharge, a dramatic decline from 753 m^2 g^{-1} to 65.8 m^2 g^{-1} is observed, supporting the proposed mobile carbon mechanism of graphitization during FJH.[21] Conversely, CaO would reside along pores, reinforcing the pores against closure during the high-temperature bond reconstruction. In the case of HC FJH of already high surface area amorphous carbon such as Cabot BP-2000 carbon black (~1500 m^2 g^{-1}), a significant decrease in surface area is observed (200 m^2 g^{-1}) similar to when azodicarbonamide is used as an activating agent. This is because the azodicarbonamide is fully degraded during the LC discharge, leaving no proppants behind to preserve the pores. Similarly, when the CaO residue is rinsed away before the HC discharge, little to no porosity is observed, and a low surface area is obtained (Figure S12), again indicative that the mobile carbon during high-temperature graphitization leads to closure of micropores and collapse of the wrinkled sheet structure. PET feedstocks do not convert to HWFG since the melting point of PET is significantly higher than the degradation temperature of the $Ca(OAc)_2$. There is no physical activation, producing no hierarchical porosity. A proposed schematic for the mechanism is shown in Figure 4.

There is little literature on turbostratic graphene or HWG structures, and to our knowledge only one literature report analyzes a material that is characterized as porous and turbostratic.[42] High-resolution single Raman spectra are shown for HWFG synthesized from different feedstocks in Figure 5a. A high D/G peak intensity ratio most often results from the formation of poor-quality graphene with low crystallinity, small sheet size, and high defect concentration.[31] However, we observe a large D/G ratio of 0.7−0.8, despite the very high 2D/G ratio of up to 3.24 (Figure 5b). A high 2D/G ratio is associated with high sp^2-hybridization and long-range order, while a 2D peak fitted with a single Lorentzian is indicative of a single layer or spectroscopically decoupled layers of graphene.[43] It seems counterintuitive that a high D/G ratio (0.7−0.8) and high 2D/G ratio (up to 3.24) can be simultaneously observed: one is indicative of high disorder, while the other is indicative of long-range intrasheet order. However, for HWFG, we observe these features that could indicate large, well-formed, spectroscopically decoupled graphene sheets that are penetrated with pores, causing edge and point defects. A noticeable D′ peak is also observed at ~1630 cm^{-1}, indicative of armchair edge types being present and confirming the presence of defects within the sheets. The D′ peak is spectroscopic evidence of strained or suspended graphene sheets, which could be occurring in the HWFG material at locations with 3D pores or wrinkles.[44] The identity of the D′ peak was confirmed using variable excitation wavelength Raman spectroscopy (Figure 5c), which showed peak dispersion as a function of excitation wavelength, matching well with literature values.[25]

Rather than relying on a single high-resolution spectrum such as Figure 5b to demonstrate the holey and wrinkled arrangement of the graphene sheets, we carried out statistical

https://doi.org/10.1021/acsnano.2c00379

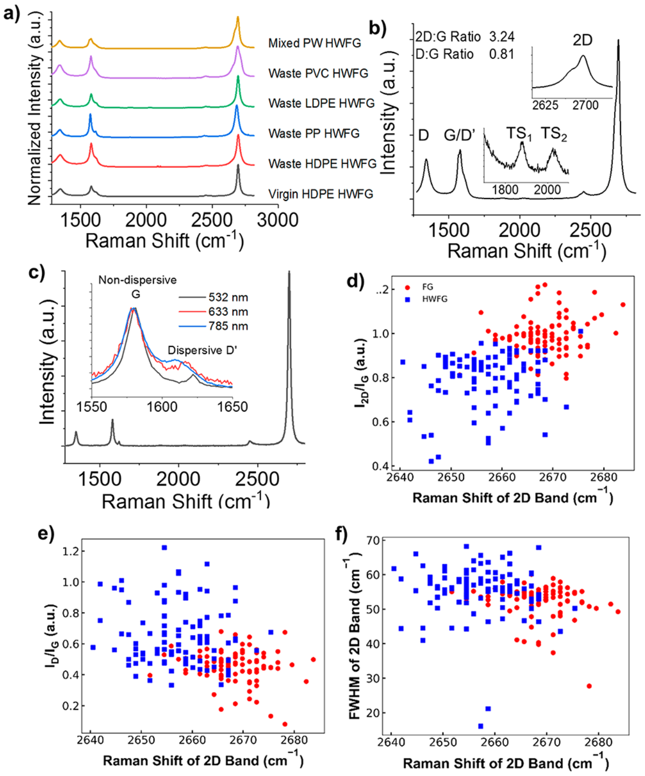

Figure 5. High-resolution Raman characterization of the HWFG. (a) Raman spectra of HWFG derived from various plastic sources. (b) Unusual Raman spectra showing simultaneously high D/G and 2D/G ratios, as well as turbostratic stacking but a multi-Lorentzian fit 2D peak. This unusual behavior may indicate wrinkling resulting in many different spectroscopic environments occurring in a small area. (c) Variable excitation wavelength Raman spectroscopy probing the dispersive character of the D′ peak and nondispersive nature of the G peak. (d−f) Heat maps of 100 Raman spectra comparing the 2D/G ratio, D/G ratio, and 2D fwhm as a function of the 2D peak location. Blue dots represent HWFG spectra, and red dots represent FG spectra.

analysis of 100 randomly selected spectra to compare FG to HWFG (Figure 5d−f). Comparing HWFG to FG, significant differences in fwhm and position of the 2D peak can be observed, even for spots of HWFG and FG that have similar 2D/G ratios. Each dot is a spectrum from a Raman spectral map. It is known that wrinkling and a small difference in height (<10 nm) can result in large shifts in the 2D peak position, up to 70 cm^{-1}, and that the observed variation of the 2D peak position is related to variations in the orientational properties of graphene.[45] For HWFG, the 2D peak is observed over a 35 cm^{-1} range, whereas the FG has a range of 20 cm^{-1}. The fwhm of the 2D peak also has a much larger range in the HWFG (55 cm^{-1}) than in the FG sample (35 cm^{-1}). This analysis demonstrates that significant wrinkling may be taking place in the bulk of the HWFG samples, as well as an increase in intersheet defects as evidenced by the increased D/G ratio (Figure 5e).

In addition, we observe another interesting and possibly unreported phenomena, the presence of the TS$_1$ and TS$_2$ peaks occurring simultaneously with a multifunctional 2D peak. When graphene is graphitically stacked, the 2D peak weakens in intensity and can be fit by four or more distinct Lorentzian functions.[31] As shown in Figure 5b, we observe the TS$_1$ and TS$_2$ peaks that are indicative of rotational disorder and spectroscopic decoupling of graphene layers and no graphitic stacking occurring in the turbostratic HWFG as discussed.[46] With turbostratic graphene, these peaks are observed, and the M peak at 1750 cm^{-1}, an indicator of ordered graphitic stacking, is silent.[46] Thus, the spectra indicate that HWFG is not graphitically stacked, while the multifunctional 2D peak indicates graphitic stacking, although the very high intensity of the 2D peak again indicates a lack of order and pseudo-single-sheet arrangements. This might be spectroscopic evidence of the 3D pores formed at the interfaces of graphene sheets, where some regions of a sheet are graphitically stacked with neighboring sheets, while other regions of the sheets are disordered due to wrinkling. Taken together, the interesting Raman spectra results: high D/G ratio despite high 2D/G ratio, multifunctional 2D peak with remaining TS$_1$/TS$_2$ peaks, and the strong and dispersive D′ peak further distinguish HWFG from normal FG.

We sought to show the utility of the HWFG though not seeking to exceed the performance of all reported examples of graphenes. Because of the high concentration of pores and edge defects within the HWFG sheets, it was hypothesized that HWFG could have a high activity as an electrocatalyst. Significant literature demonstrates that defective, conductive carbon has a high catalytic activity since the defects disrupt the band structure.[47] Further, transition-metal-free electrocatalysts are of interest due to low costs and higher stabilities.[48] The hydrogen evolution reaction (HER) is important for fuel-cell technology. The HER activity of HDPE-derived HWFG shows an overpotential of 613 mV versus RHE under acidic conditions, significantly lower than that of FG (776 mV) or graphite (Figure 6a). A high surface area and hierarchical porous structure allows for the evolved gas to escape the catalytic surface, maintaining stable production over time. A Tafel slope of 91 mV decade^{-1} was observed, showing a high and efficient exchange current density (Figure 6b). Measurement of the electrochemical surface area is possible through determination of the capacitance of the system; an electrochemical surface area of 43 cm^2 of catalyst per cm^2 of electrode was measured, attributable to the high surface area of HWFG (Figure 6c). Because of the transition-metal-free nature of the HWFG, excellent stability is observed, with the overpotential decreasing by 19 mV over 20 h of testing while being maintained at −20 mA cm^{-2} (Figure 6d). Since transition metals were never used in the synthesis or workup, they are not present to dissipate or convert to nonactive oxidized states. Therefore, the HWFG maintains a constant activity, and the overpotential decreases slightly due to the cavitation of hydrogen gas being produced, increasing the defects present in the HWFG.[49] The HER activity is compared to 14 other recent metal-free catalysts in Table S2. Virgin HDPE-derived HWFG outperforms some doped graphenes and is within 40−80 mV of other 3D porous and defective graphenes that have more difficult synthetic processes.

Lithium metal batteries, though promising due to their high energy densities, suffer from poor stability that results from plating or dendrite formation, leading to self-discharge, short circuits, and sometimes catastrophic failure. HWFG might allow for easier and more rapid intercalation of lithium ions due to its porosity. Similarly, the high surface area might lower the overpotential and increase the energy density. The HWFG with larger surface area and microporous structure was determined to facilitate the electrodeposition of Li-metal since there is a lower local current density under the same

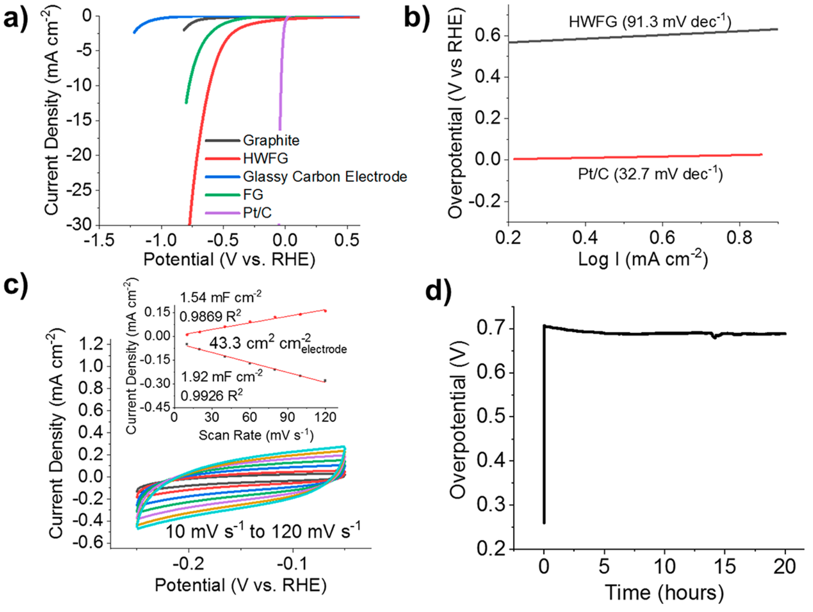

Figure 6. HER electrochemical activity of mixed PW HWFG including (a) linear scan voltammograms, (b) Tafel slope, (c) capacitance determination (The inset shows the current density as the scan rate is varied), and (d) stability testing of HDPE-derived HWFG held at −20 mA/cm^2.

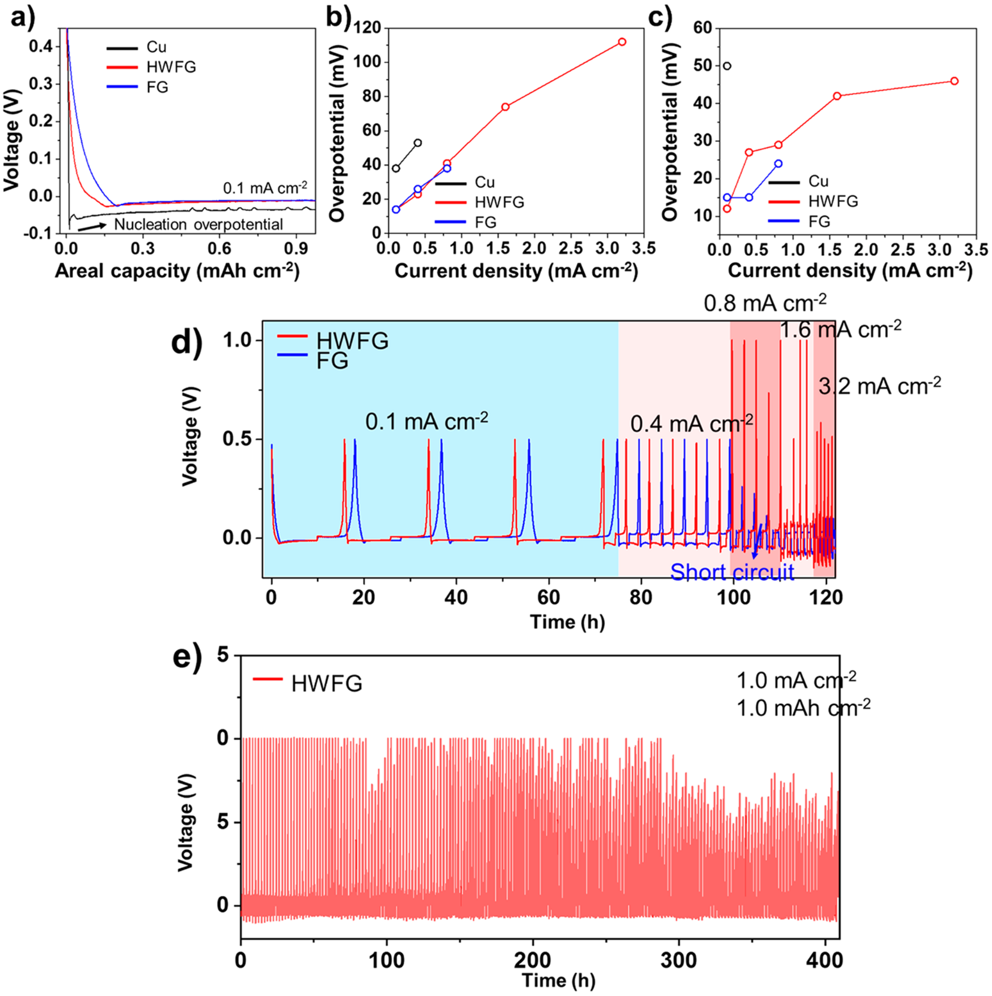

Figure 7. Electrochemical performance of HWFG. (a) Voltage profile at 0.1 mA cm^{-2}. (b) Onset and (c) steady overpotentials of Cu, FG, and HWFG at different current densities. The area capacity is 1 mAh cm^{-2}. (d) Voltage profiles of Cu, FG, and HWFG at different current densities. The area capacity is 1 mAh cm^{-2}. (e) Voltage profiles of Cu, FG, and HWFG at 1 mA cm^{-2}. The area capacity is 1 mAh cm^{-2}.

apparent current densities for the electrode. Therefore, a low nucleation overpotential and steady overpotential at a low current density of 12 and 14 mV at 0.1 mA cm^{-2}, respectively, for HWFG; 15 and 14 mV, respectively, for FG; and 50 and 38 mV, respectively, for Cu are shown in Figure 7a. The effect is more notable under higher current densities as shown in Figure 7b,c. At >1.0 mA cm^{-2}, the batteries with Cu or FG as anodes suffer short circuits, presumably because of uneven Li deposition and formation of Li dendrites, while the HWFG has a superior electrochemical performance with a low overpotential even at 3.2 mA cm^{-2} (Figure 7d). The low nucleation overpotential of 46 mV and steady overpotential of 112 mV are comparable to other carbonaceous materials.[50−52] The voltage profile of HWFG at 1.0 mA cm^{-2} with a total capacity of 1.0 mAh cm^{-2} is shown in Figure 7e; there is a stable overpotential in the first 200 cycles, which demonstrates the utility of HWFG as anodes in Li-metal batteries.

CONCLUSIONS

We present a rapid and scalable method to produce high-quality HWFG from mixed PW using FJH. The porosity produces interesting spectroscopic features. The HWFG with high surface area and defect concentration is found to be effective as a metal-free HER electrocatalyst, Li-metal battery anode, and CO_2 gas adsorption material. The ease of synthesis, combined with competitive properties in multiple applications, demonstrates a pathway to bulk and scalable synthesis of HWFG, with minimal steps and greatly reduced resource use. We plan to further demonstrate the scalability of this method as well as explore heteroatom-doped HWFG, which may result in increased bandgaps.

EXPERIMENTAL SECTION

Chemicals and Materials. Pluronic F-127 (Millipore-Sigma), virgin HDPE powder (grain size 35 μm, Millipore-Sigma), amorphous carbon black Pearls BP-2000 (Cabot), metallurgical coke (SunCoke), and Nafion 417 perfluorinated resin (Millipore-Sigma) were used as received. PW was collected from household waste, including carbonated beverage bottles, milk jugs, metal-free PVC plumbing pipes, grocery bags, food packaging, and coffee cups. PW was ground using a hammer mill (CGoldenWall, model DF-15) and was sieved to only use particles smaller than 0.6 mm (#30 sieve).

Synthesis of HWFG. HWFG was synthesized using a custom-fabricated FJH system (more details in the Supporting Information). In brief, finely ground PW (0.65 g) was mixed with $Ca(OAc)_2$ (1.95 g) and amorphous carbon black BP-2000 (0.165 g) or metallurgical coke (0.125 g) using a mortar and pestle. The resulting gray powder mixture (2.77 g) was placed in a quartz tube (12 mm internal diameter) with a tight-fitting spring around the tube to keep it under compression. Graphite electrodes are then placed at the ends of the tube to contain the powder, and the tube was placed between metal screw electrodes connecting it to the FJH system. The metal was not ever in contact with the sample. Four small notches (1 mm^2) were cut in one of the graphite electrodes to allow for volatiles to outgas during the FJH process so that the quartz tube will not shatter. The powder sample was compressed between the graphite electrodes until a resistance across the sample of 1.5 kΩ was reached. An LC discharge was then applied at a constant 208 V, with current increasing from 0.1 A to ∼25 A, for 50 s. Extensive outgassing of decomposing salt and flammable carbonizing plastic was noted, so care should be taken to vent the reaction chamber with a rapid purge of air during carbonization. Because of the evolution of gases during the FJH process, both from the volatilization of the plastics as well as the degradation of the salt, it is important that the electrodes have frits to equalize the pressure, which prevents expansion inside the tube from disconnecting the circuit and interrupting the current discharge. Further, springs pushing the electrodes inward during the FJH discharge maintain contact between the electrodes, sample, and power source (Figure S1d). Unlike other FJH procedures, no vacuum desiccator was used but rather a purge of air to remove the outgassing volatiles through the fume hood. Then, an HC flash with a short-duration current discharge supplied by 140 μF capacitors that were charged to 120 V and discharged for 250 ms was passed through the sample. The resulting HWFG product (∼0.4 g) can then be extruded from the quartz tube and soaked in 100 mL of dilute acid (1 M acetic or HCl) to remove the CaO residue. The HWFG was then filtered using a vacuum filtration flask with a PVDF filter membrane of 0.45 μm pores. The HWFG was rinsed with 500 mL of deionized water and gently scraped off the filter membrane. The HWFG powder was then dried overnight in an oven at 150 °C. The yield of HWFG varied based on the plastic feedstock, ranging from 0.325 g for virgin HDPE to as low as 0.251 g for waste PVC. The carbon content of the PW feedstock determines the theoretical maximum yield of carbon that can be converted into HWFG following the carbonization and graphitization steps. Thus, it can be expected that since chlorine in PVC reduces the overall amount of carbon present in the feedstock, the yields will be lower. Calcium acetate is 30.4% carbon; however, as we observe, the carbon originating from the $Ca(CO_3)$ leaves the system in the form of acetone and CO_2. This leaves the carbon from the polymeric feedstocks to be converted into graphene. Assuming HDPE is 86% carbon and carbon black is 100% carbon in the 2.77 g of starting material mixture ($Ca(OAc)_2$, HDPE, and amorphous carbon), there is only 0.753 g of carbon available to be converted into the HWFG. Thus, the yields of up to 0.325 g represent 43% of the maximum theoretical yield.

It has been previously observed that the yield of the graphene produced by the LC FJH of plastics can be correlated with the ultimate thermal stability of the feedstock.[22] For example, PVC with a thermal stability of 200 °C gives a lower yield than HDPE with a thermal stability of 460 °C. Oligomers are produced when the polymer is above the point of the thermal stability, resulting in a reduced yield. Since the initial current is low during the LC step, the heating rates are slower at the start of the discharge. With more thermally stable plastics, there is a shorter amount of time for oligomers to evolve as the product is converted into the high surface area amorphous carbon, resulting in higher yields. However, as discussed with the PET example, the HWFG surface area also depends on the melting temperature of the polymer. TGA is a powerful tool to determine if a waste plastic mixture is a good candidate for the FJH upcycling into HWFG. To better understand the specifics of the polymer feedstocks and improve reproducibility, we have carried out TGA on all polymer feedstock as well as Fourier transform infrared (FTIR) analyses. This characterization is shown in Figures S13 and S14. Thermal stabilities above the degradation point of the calcium acetate salt are observed for all polymers. This thermal stability is important as the calcium acetate degrades to evolve acetone at ∼200 °C, forming the macropores, and if the carbonization has already occurred, then a significantly decreased surface area would be expected. Similar thermal stabilities are observed for these waste polymers when compared to reported literature values of pure virgin polymer samples.[22] Some inorganic contaminants are present in the waste LDPE and PVC samples as demonstrated by the incomplete degradation of these samples, with 5−10 wt % remaining after analysis. These inorganic contaminants may be nanoclays or other composite materials, which are not present in literature data of pure virgin polymer samples.[22] As demonstrated by the TGA of the HWFG, these contaminants are removed during the FJH process; however, it is yet unknown if and how these contaminants impact the mechanism of HWFG synthesis or overall surface area of the product. FTIR of the waste plastic samples used in this study very closely match spectra found in the literature.[22] This is indicative of the waste polymers having relatively high purity of the organic components and minimal spectral presence of dyes or plasticizers. These dyes, plasticizers, adhesives, food waste, and fillers, if present, are converted into graphene due to the high temperatures achieved to break the molecular bonds present, subliming out non-carbon atoms.

https://doi.org/10.1021/acsnano.2c00379
ACS Nano XXXX, XXX, XXX−XXX

With our current lab-scale reactor, we are limited to 2.75 g of starting material mixture due to the peak current and voltage of the LC step. We initially began this process using a standard wall outlet (120 V/15 A) before switching to a dedicated three-phase 208 V/25 A power source. With a more powerful sustained LC power source, such as a 30 kVA three-phase, 480 V current source, it is possible that larger scales of production could be realized. The HC discharge step is largely only limited by the amount of capacitance used in the capacitor bank, so this can readily be scaled to accommodate larger production scales.

Characterization and Measurements. Raman spectra were collected using a Renishaw inVia Raman microscope outfitted with a 5 mW 532 nm laser, 5 mW 633 laser, and 5 mW 785 nm laser. A 50× objective lens was used to collect all spectra. Analysis of Raman spectra, including peak intensity ratios, utilize the height of the peak. XPS data were collected using a PHI Quantera SXM scanning X-ray microprobe with a base pressure of 5×10^{-9} Torr. Survey spectra were recorded using 0.5 eV step sizes with a pass energy of 140 eV. Elemental spectra were recorded using 0.1 eV step sizes with a pass energy of 26 eV. All of the XPS spectra were corrected using the C 1s peaks (284.6 eV) as reference. TGA thermograms were collected using a TA Instruments Q-600 Simultaneous TGA/DSC using alumina pans, with a heating rate of 10 °C min^{-1} up to 780 °C. Air atmosphere at a flow rate of 80 mL/min was used to purge the sample chamber. Powder XRD spectra were collected using a Rigaku SmartLab II using zero background sample holders at a scan rate of 1°/min and a 0.05° step size. BET surface area analysis was carried out using a Quantachrome Autosorb-iQ3-MP/Kr BET surface analyzer, using nitrogen as the analysis gas. Samples were degassed for 12 h at 200 °C under a high vacuum prior to analysis. SEM images were taken with a FEI Helios Nanolab 660 dual beam SEM system. A voltage of 10 keV was employed in imaging. TEM and SAED images were obtained on a JEOL 2100 field emission transmission electron microscope at an acceleration voltage of 200 kV. Samples were prepared by drop casting extremely dilute HWFG/ethanol solutions onto lacey carbon grids. HWFG was dispersed in a 1% surfactant aqueous solution using Pluronic-F127, a nonionic polyol surfactant. Varying amounts of ground HWFG powder were weighed into centrifuge tubes, and solvent was added to yield the initial loading concentration (∼1 mg HWFG powder/mL of solvent). The centrifuge tubes were then sonicated in a cup-horn sonicator for 10 min (Cole-Parmer Qsonica 448) and centrifuged at 550 relative centrifugal force for 5 min to remove larger aggregates. The supernatant was decanted after centrifugation and diluted 100× since the graphene concentration leads to a very high absorbance. The absorbance of the solution was measured at 660 nm. The graphene concentration was determined using Beer's law with an extinction coefficient of 66 L g^{-1} cm^{-1}. Quartz cuvettes with simultaneous baseline correction were used. Electrocatalytic tests were performed in an electrochemical cell using a glassy carbon electrode 5 mm in diameter. The HWFG (1.0 mg) and 5 wt % Nafion solution (80 μL) were mixed in ethanol (1.60 mL) and water (6.40 mL) followed by 4 h bath sonication (Cole-Parmer, model 08849-00) to obtain a homogeneous ink. A 16.00 μL amount of as-prepared catalyst ink was loaded onto the electrode and dried in air at room temperature. Electrochemical tests were carried out using a CHI 608D electrochemical workstation (CHInstruments, Inc.) with a three-electrode configuration. A graphite rod and a HgO/Hg electrode were used as the counter electrode and reference electrode, respectively. Acidic aqueous conditions, purged with bubbled Ar gas prior to testing, were used. The electrochemical surface area (ECSA) is calculated from the electrochemical double-layer capacitance (C_{dl}) of the catalyst. C_{dl} was determined from the slope by plotting current density as a function of scan rate in a potential range where no Faradaic current was generated. The ECSA was calculated from eq 1:

$$\mathrm{ECSA} = C_{\mathrm{dl}}/C_{\mathrm{s}} \tag{1}$$

where C_{s} is the specific capacitance of a flat standard electrode with 1 cm^2 of real surface area. The value of C_{s} is determined to be 40 μF cm^{-2} according to several previous studies.[53−55]

Gas Adsorption Measurements. CO_2 uptake measurements were performed on a Setaram PCT Pro using ultrapure grade CO_2 from 0 to 1 Ω at 0.06 bar increments.

Electrochemical Tests. In half-cell tests, the plating and stripping measurements were HWFG. The control experiments used bare Cu foils or Cu metal foils covered by FG. The area of the Li foils was ∼2 cm^2. The electrolyte used was 1 M LiTFSI in a mixture of DME and DOL (v/v = 1:1) with 2% $LiNO_3$ as the additive. A lean electrolyte condition was applied here; the volume in each battery was 30 μL. The separator was Celgard K2045. The batteries were prepared inside an Ar-filled glovebox (O_2 content <0.3 ppm, H_2O content <0.5 ppm). The tests were conducted at constant currents from 0.5 to 3.2 mA cm^{-2}. The areal capacity was determined by the time for the charge/discharge process and varied from 1 to 2 mAh cm^2. For the starting overpotential test, the difference between the lowest transient potential and the steady cycling potential was used for comparison of the respective current densities.

ASSOCIATED CONTENT

Supporting Information

The Supporting Information is available free of charge at https://pubs.acs.org/doi/10.1021/acsnano.2c00379.

> Circuit diagram, heater assembly considerations, additional Raman spectra, BET isotherms, SEM images, and other graphs, spectra, and a table comparing other metal-free HER catalysts (PDF)

AUTHOR INFORMATION

Corresponding Author

James M. Tour − *Department of Chemistry and Smalley-Curl Institute, NanoCarbon Center, Welch Institute for Advanced Materials, Department of Materials Science and NanoEngineering, Rice University, Houston, Texas 77005, United States;* orcid.org/0000-0002-8479-9328; Email: tour@rice.edu

Authors

Kevin M. Wyss − *Department of Chemistry, Rice University, Houston, Texas 77005, United States*

Weiyin Chen − *Department of Chemistry, Rice University, Houston, Texas 77005, United States;* orcid.org/0000-0002-6427-4129

Jacob L. Beckham − *Department of Chemistry, Rice University, Houston, Texas 77005, United States*

Paul E. Savas − *Department of Chemistry, Rice University, Houston, Texas 77005, United States*

Complete contact information is available at: https://pubs.acs.org/10.1021/acsnano.2c00379

Notes

The authors declare the following competing financial interest(s): Universal Matter Inc. has licensed from Rice University the FJH approach to graphene. J.M.T. is a stockholder in Universal Matter, but not an employee, officer, or director. Potential conflicts of interest are mitigated through regular disclosures to and compliance with Rice University's Office of Sponsored Programs and Research Compliance.

ACKNOWLEDGMENTS

K.M.W. and J.L.B. acknowledge the NSF GRFP for generous funding of the research. This research was supported by the Air Force Office of Scientific Research (FA9550-19-1-0296) and the Army Corps of Engineers - ERDC (W912HZ-21-2-0050). The authors acknowledge the use of the Electron Microscopy

Center (EMC) at Rice University. We thank Dr. Bo Chen for his help with XPS data analysis.

REFERENCES

(1) Ye, R.; Tour, J. M. Graphene at Fifteen. *ACS Nano* **2019**, *13*, 10872−10878.

(2) Balandin, A. A.; Ghosh, S.; Bao, W.; Calizo, I.; Teweldebrhan, D.; Miao, F.; Lau, C. N. Superior Thermal Conductivity of Single-Layer Graphene. *Nano Lett.* **2008**, *8*, 902−907.

(3) Abergel, D. S. L.; Apalkov, V.; Berashevich, J.; Ziegler, K.; Chakraborty, T. Properties of Graphene: A Theoretical Perspective. *Adv. Phys.* **2010**, *59*, 261−482.

(4) Lee, C.; Wei, X.; Kysar, J. W.; Hone, J. Measurement of the Elastic Properties and Intrinsic Strength of Monolayer Graphene. *Science* **2008**, *321*, 385−388.

(5) Kumar, A.; Sharma, K.; Dixit, A. R. A Review of the Mechanical and Thermal Properties of Graphene and Its Hybrid Polymer Nanocomposites for Structural Applications. *J. Mater. Sci.* **2019**, *54*, 5992−6026.

(6) Nag, A.; Mitra, A.; Mukhopadhyay, S. C. Graphene and Its Sensor-Based Applications: A Review. *Sens. Actuators, A* **2018**, *270*, 177−194.

(7) Olabi, A. G.; Abdelkareem, M. A.; Wilberforce, T.; Sayed, E. T. Application of Graphene in Energy Storage Device − A Review. *Renewable Sustainable Energy Rev.* **2021**, *135*, 110026.

(8) Wu, Y.; Zhu, J.; Huang, L. A Review of Three-Dimensional Graphene-Based Materials: Synthesis and Applications to Energy Conversion/Storage and Environment. *Carbon* **2019**, *143*, 610−640.

(9) Cao, Y.; Fatemi, V.; Fang, S.; Watanabe, K.; Taniguchi, T.; Kaxiras, E.; Jarillo-Herrero, P. Unconventional Superconductivity in Magic-Angle Graphene Superlattices. *Nature* **2018**, *556*, 43−50.

(10) Kun, P.; Kukucska, G.; Dobrik, G.; Koltai, J.; Kürti, J.; Biró, L. P.; Tapasztó, L.; Nemes-Incze, P. Large Intravalley Scattering Due to Pseudo-Magnetic Fields in Crumpled Graphene. *npj 2D Mater. Appl.* **2019**, *3*, 1−7.

(11) Naumis, G. G.; Barraza-Lopez, S.; Oliva-Leyva, M.; Terrones, H. Electronic and Optical Properties of Strained Graphene and Other Strained 2D Materials: A Review. *Rep. Prog. Phys.* **2017**, *80*, 096501.

(12) Guirguis, A.; Maina, J. W.; Zhang, X.; Henderson, L. C.; Kong, L.; Shon, H.; Dumée, L. F. Applications of Nano-Porous Graphene Materials − Critical Review on Performance and Challenges. *Mater. Horiz.* **2020**, *7*, 1218−1245.

(13) Li, C.; Zhang, X.; Wang, K.; Sun, X.; Liu, G.; Li, J.; Tian, H.; Li, J.; Ma, Y. Scalable Self-Propagating High-Temperature Synthesis of Graphene for Supercapacitors with Superior Power Density and Cyclic Stability. *Adv. Mater.* **2017**, *29*, 1604690.

(14) Zhang, Y.; Wan, Q.; Yang, N. Recent Advances of Porous Graphene: Synthesis, Functionalization, and Electrochemical Applications. *Small* **2019**, *15*, 1903780.

(15) Tao, Y.; Sui, Z.-Y.; Han, B.-H. Advanced Porous Graphene Materials: From in-Plane Pore Generation to Energy Storage Applications. *J. Mater. Chem. A* **2020**, *8*, 6125−6143.

(16) Jiang, L.; Fan, Z. Design of Advanced Porous Graphene Materials: From Graphene Nanomesh to 3D Architectures. *Nanoscale* **2014**, *6*, 1922−1945.

(17) Dong, L.; Yang, J.; Chhowalla, M.; Loh, K. P. Synthesis and Reduction of Large Sized Graphene Oxide Sheets. *Chem. Soc. Rev.* **2017**, *46*, 7306−7316.

(18) Serrano-Luján, L.; Víctor-Román, S.; Toledo, C.; Sanahuja-Parejo, O.; Mansour, A. E.; Abad, J.; Amassian, A.; Benito, A. M.; Maser, W. K.; Urbina, A. Environmental Impact of the Production of Graphene Oxide and Reduced Graphene Oxide. *SN Appl. Sci.* **2019**, *1*, 179.

(19) Chang, J.-H.; Hung, Y.-H.; Luo, X.-F.; Huang, C.-H.; Jung, S.; Chang, J.-K.; Kong, J.; Su, C.-Y. The Hierarchical Porosity of a Three-Dimensional Graphene Electrode for Binder-Free and High Performance Supercapacitors. *RSC Adv.* **2016**, *6*, 8384−8394.

(20) Zhao, J.; Tang, Z.; Qiu, Y.; Gao, X.; Wan, J.; Bi, W.; Shen, S.; Yang, J. Porous Crumpled Graphene with Improved Specific Surface Area Based on Hydrophilic Pre-Reduction and Its Adsorption Performance. *J. Mater. Sci.* **2019**, *54*, 8108−8120.

(21) Luong, D. X.; Bets, K. V.; Algozeeb, W. A.; Stanford, M. G.; Kittrell, C.; Chen, W.; Salvatierra, R. V.; Ren, M.; McHugh, E. A.; Advincula, P. A.; Wang, Z.; Bhatt, M.; Guo, H.; Mancevski, V.; Shahsavari, R.; Yakobson, B. I.; Tour, J. M. Gram-Scale Bottom-up Flash Graphene Synthesis. *Nature* **2020**, *577*, 647−651.

(22) Algozeeb, W. A.; Savas, P. E.; Luong, D. X.; Chen, W.; Kittrell, C.; Bhat, M.; Shahsavari, R.; Tour, J. M. Flash Graphene from Plastic Waste. *ACS Nano* **2020**, *14*, 15595−15604.

(23) Wyss, K. M.; Beckham, J. L.; Chen, W.; Luong, D. X.; Hundi, P.; Raghuraman, S.; Shahsavari, R.; Tour, J. M. Converting Plastic Waste Pyrolysis Ash into Flash Graphene. *Carbon* **2021**, *174*, 430−438.

(24) Shallcross, S.; Sharma, S.; Kandelaki, E.; Pankratov, O. A. Electronic Structure of Turbostratic Graphene. *Phys. Rev. B* **2010**, *81*, 165105.

(25) Wyss, K. M.; Wang, Z.; Alemany, L. B.; Kittrell, C.; Tour, J. M. Bulk Production of Any Ratio ^{12}C:^{13}C Turbostratic Flash Graphene and Its Unusual Spectroscopic Characteristics. *ACS Nano* **2021**, *15*, 10542−10552.

(26) Advincula, P. A.; Luong, D. X.; Chen, W.; Raghuraman, S.; Shahsavari, R.; Tour, J. M. Flash Graphene from Rubber Waste. *Carbon* **2021**, *178*, 649−656.

(27) Ghosh, A.; Subrahmanyam, K. S.; Krishna, K. S.; Datta, S.; Govindaraj, A.; Pati, S. K.; Rao, C. N. R. Uptake of H_2 and CO_2 by Graphene. *J. Phys. Chem. C* **2008**, *112*, 15704−15707.

(28) Choe, K. H.; Lee, D. S.; Seo, W. J.; Kim, W. N. Properties of Rigid Polyurethane Foams with Blowing Agents and Catalysts. *Polym. J.* **2004**, *36*, 368−373.

(29) Gao, Y.; Yue, Q.; Gao, B.; Li, A. Insight into Activated Carbon from Different Kinds of Chemical Activating Agents: A Review. *Sci. Total Environ.* **2020**, *746*, 141094.

(30) Jalilov, A. S.; Li, Y.; Kittrell, C.; Tour, J. M. Increased CO_2 Selectivity of Asphalt-Derived Porous Carbon through Introduction of Water into Pore Space. *Nat. Energy* **2017**, *2*, 932−938.

(31) Merlen, A.; Buijnsters, J. G.; Pardanaud, C. A Guide to and Review of the Use of Multiwavelength Raman Spectroscopy for Characterizing Defective Aromatic Carbon Solids: From Graphene to Amorphous Carbons. *Coatings* **2017**, *7*, 153.

(32) Zhang, W.; Liu, L.; Li, Y.; Wang, D.; Ma, H.; Ren, H.; Shi, Y.; Han, Y.; Ye, B.-C. Electrochemical Sensing Platform Based on the Biomass-Derived Microporous Carbons for Simultaneous Determination of Ascorbic Acid, Dopamine, and Uric Acid. *Biosens. Bioelectron.* **2018**, *121*, 96−103.

(33) Bhat, V. S.; S, S.; Hegde, G. Review—Biomass Derived Carbon Materials for Electrochemical Sensors. *J. Electrochem. Soc.* **2020**, *167*, 037526.

(34) Xie, X.; Wang, M.; Han, J. Assessment of Fuel-Cycle Energy Use and Greenhouse Gas Emissions for Fischer−Tropsch Diesel from Coal and Cellulosic Biomass. *Environ. Sci. Technol.* **2011**, *45*, 3047−3053.

(35) Arvidsson, R.; Molander, S.; Sandén, B. A. Review of Potential Environmental and Health Risks of the Nanomaterial Graphene. *Human Ecological Risk Assess: Int. J.* **2013**, *19*, 873−887.

(36) Arvidsson, R.; Kushnir, D.; Sandén, B. A.; Molander, S. Prospective Life Cycle Assessment of Graphene Production by Ultrasonication and Chemical Reduction. *Environ. Sci. Technol.* **2014**, *48*, 4529−4536.

(37) Wyss, K. M.; Luong, D. X.; Tour, J. M. Large-Scale Syntheses of 2D Materials: Flash Joule Heating and Other Methods. *Adv. Mater.* **2022**, *34*, 2106970.

(38) Robledo-Ortiz, J. R.; Zepeda, C.; Gomez, C.; Rodrigue, D.; González-Núñez, R. Non-Isothermal Decomposition Kinetics of Azodicarbonamide in High Density Polyethylene Using a Capillary Rheometer. *Polym. Test.* **2008**, *27*, 730−735.

(39) Wan, L.; Chen, W.; Xu, H.; Wang, Y.; Yuan, J.; Zhou, Z.; Sun, S. A Mild CO_2 Etching Method to Tailor the Pore Structure of Platinum-Free Oxygen Reduction Catalysts in Proton Exchange

Membrane Fuel Cells. *ACS Appl. Mater. Interfaces* **2021**, *13*, 45661−45669.

(40) Zhou, Y.; Hong, L. The Growth of Porous Carbon Fibres through *in Situ* Vapour Deposition. *RSC Adv.* **2013**, *3*, 19769−19773.

(41) Alcañiz-Monge, J.; Cazorla-Amorós, D.; Linares-Solano, A.; Yoshida, S.; Oya, A. Effect of the Activating Gas on Tensile Strength and Pore Structure of Pitch-Based Carbon Fibres. *Carbon* **1994**, *32*, 1277−1283.

(42) Strauss, V.; Marsh, K.; Kowal, M. D.; El-Kady, M.; Kaner, R. B. A Simple Route to Porous Graphene from Carbon Nanodots for Supercapacitor Applications. *Adv. Mater.* **2018**, *30*, 1704449.

(43) Kim, K.; Coh, S.; Tan, L. Z.; Regan, W.; Yuk, J. M.; Chatterjee, E.; Crommie, M. F.; Cohen, M. L.; Louie, S. G.; Zettl, A. Raman Spectroscopy Study of Rotated Double-Layer Graphene: Misorientation-Angle Dependence of Electronic Structure. *Phys. Rev. Lett.* **2012**, *108*, 246103.

(44) Wu, J.-B.; Lin, M.-L.; Cong, X.; Liu, H.-N.; Tan, P.-H. Raman Spectroscopy of Graphene-Based Materials and Its Applications in Related Devices. *Chem. Soc. Rev.* **2018**, *47*, 1822−1873.

(45) Robinson, J. A.; Puls, C. P.; Staley, N. E.; Stitt, J. P.; Fanton, M. A.; Emtsev, K. V.; Seyller, T.; Liu, Y. Raman Topography and Strain Uniformity of Large-Area Epitaxial Graphene. *Nano Lett.* **2009**, *9*, 964−968.

(46) Jorio, A.; Cançado, L. G. Raman Spectroscopy of Twisted Bilayer Graphene. *Solid State Commun.* **2013**, *175*−*176*, 3−12.

(47) Younis, M. A.; Lyu, S.; Zhao, Q.; Lei, C.; Zhang, P.; Yang, B.; Li, Z.; Lei, L.; Hou, Y.; Feng, X. Noble Metal-Free Two Dimensional Carbon-Based Electrocatalysts for Water Splitting. *BMC Materials* **2019**, *1*, 6.

(48) Ali, A.; Shen, P. K. Recent Progress in Graphene-Based Nanostructured Electrocatalysts for Overall Water Splitting. *Electrochem. Energy Rev.* **2020**, *3*, 370−394.

(49) García-Miranda Ferrari, A.; Brownson, D. A. C.; Banks, C. E. Investigating the Integrity of Graphene towards the Electrochemical Hydrogen Evolution Reaction (HER). *Sci. Rep.* **2019**, *9*, 15961.

(50) Jeong, J.; Chun, J.; Lim, W.-G.; Kim, W. B.; Jo, C.; Lee, J. Mesoporous Carbon Host Material for Stable Lithium Metal Anode. *Nanoscale* **2020**, *12*, 11818−11824.

(51) Liu, Y.; Li, X.; Fan, L.; Li, S.; Maleki Kheimeh Sari, H.; Qin, J. A Review of Carbon-Based Materials for Safe Lithium Metal Anodes. *Front. Chem.* **2019**, *7*, 721.

(52) Liu, L.; Yin, Y.-X.; Li, J.-Y.; Wang, S.-H.; Guo, Y.-G.; Wan, L.-J. Uniform Lithium Nucleation/Growth Induced by Lightweight Nitrogen-Doped Graphitic Carbon Foams for High-Performance Lithium Metal Anodes. *Adv. Mater.* **2018**, *30*, 1706216.

(53) Wang, Z.; Li, Q.-K.; Zhang, C.; Cheng, Z.; Chen, W.; McHugh, E. A.; Carter, R. A.; Yakobson, B. I.; Tour, J. M. Hydrogen Peroxide Generation with 100% Faradaic Efficiency on Metal-Free Carbon Black. *ACS Catal.* **2021**, *11*, 2454−2459.

(54) Zhang, J.; Ren, M.; Wang, L.; Li, Y.; Yakobson, B. I.; Tour, J. M. Oxidized Laser-Induced Graphene for Efficient Oxygen Electrocatalysis. *Adv. Mater.* **2018**, *30*, 1707319.

(55) Zhang, C.; Sha, J.; Fei, H.; Liu, M.; Yazdi, S.; Zhang, J.; Zhong, Q.; Zou, X.; Zhao, N.; Yu, H.; Jiang, Z.; Ringe, E.; Yakobson, B. I.; Dong, J.; Chen, D.; Tour, J. M. Single-Atomic Ruthenium Catalytic Sites on Nitrogen-Doped Graphene for Oxygen Reduction Reaction in Acidic Medium. *ACS Nano* **2017**, *11*, 6930−6941.

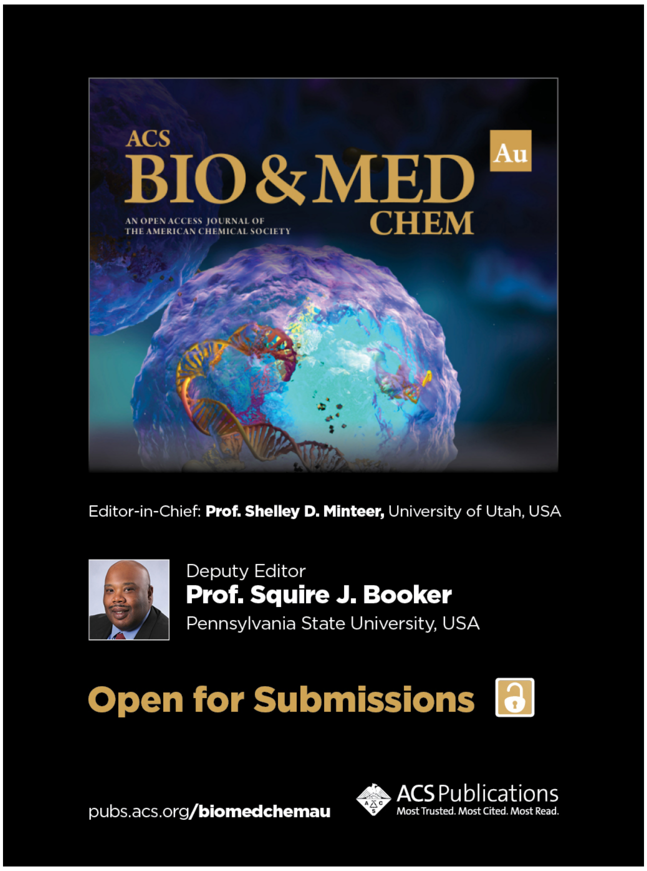

https://doi.org/10.1021/acsnano.2c00379
ACS Nano XXXX, XXX, XXX−XXX